Solar Energy Materials & Solar Cells 257 (2023) 112383

Contents lists available at ScienceDirect

Solar Energy Materials and Solar Cells

journal homepage: www.elsevier.com/locate/solmat

Design of near-ideal and omnidirectional selective solar absorber for high-temperature applications

Bowei Zhang [a,**], Lin Li [a], Sandeep Kumar Chamoli [b,*], Qi Chen [c], Xiaobin Ran [a], Kuo Zhao [a], Zhenyu Chen [a,d]

[a] Chongqing College of Electronic Engineering (CQCEE), Chongqing, 401331, China
[b] Changchun Institute of Optics, Fine Mechanics and Physics, Chinese Academy of Sciences, China
[c] College of Optoelectronic Engineering, Changchun University of Science and Technology, Changchun, Jilin, 130022, China
[d] Chongqing Institute of quality and standardization, China

A B S T R A C T

Efficient absorption of solar radiation with minimal thermal losses is required for efficient solar-to-thermal energy conversion. For this purpose, spectrally selective and omnidirectional surfaces are required that have strong, ideally unity, absorption in the solar spectral window for all incident angles and low, ideally zero, emissivity in the spectral range of blackbody radiation at operating temperature. In this article, we propose theoretically and experimentally lithographic free broadband and omnidirectional solar absorber for high-temperature applications made in a dielectric-metal-dielectric-metal fashion. We have used chromium (*Cr*), titanium (*Ti*), and tungsten (*W*) as a metal layer in the designed absorber due to their high thermal stability at high temperatures and compared their performance. The power balance equation is used to calculate the steady-state temperature considering free and forced convection conditions. *W*-based absorber shows >90% absorption in the solar window below cutoff wavelength for blackbody working at 600 K with <10% emissivity in the thermal window. Finally, we fabricate the *W*-based sample and experimentally measure the temperature rise of 100 K under one sun condition. The designed absorber can be used for several solar-thermal applications including solar-steam to electricity generation, water purification, space heating, and solar-thermal energy storage.

1. Introduction

Solar energy is a perfect alternative to fossil fuels and has the potential to fulfill ever-increasing global energy demand cleanly and sustainably. The most straightforward and direct method of harnessing solar energy is solar-to-thermal energy conversion [1–3] which requires a solar absorber to efficiently collect the sunlight. The harvested solar-thermal energy can be directly used to (i) generate electricity via thermoelectric generators [4–7], steam turbines [8], or thermophotovoltaics [9,10], (ii) purify wastewater or desalinate seawater [11], and (iii) space and/water heating [12] or can be stored in molten salts or water for off-time uses [13] and optoelectronics [14,15]. Solar absorbers are key components in all solar-thermal technologies and need to be properly designed and fabricated for a given application. Re- radiative losses from the absorber are a major limiting factor in TPV efficiency [16], therefore it is necessary to minimize the emission in the spectral range, where the blackbody radiance at the working temperature attains significant values for example blackbody radiation at 600 °C and 800 °C are most intense at 3320 nm and 2700 nm, respectively. For solar-thermo photovoltaic (TPV) systems, where the solar absorber is thermally coupled to the emitter. The absorber harvests solar-thermal energy and transfers the heat to the emitter through conduction to increase the emitter's temperature. Finally, the emitter selectively emits in a narrow wavelength matching the bandgap of a PV cell [17,18,19]. Minimization of thermal losses including radiation and convection is necessary to optimize the performance of solar-thermal systems. An ideal solar absorber should have 100% absorption with omnidirectional and polarization-independent nature in the solar spectral region so that it can harness as much energy as possible, but it should have low, ideally zero, emissivity in the spectral window of blackbody (BB) radiation [20–22]. An ideal absorber should have a sharp transition from unity absorption to zero at the transition wavelength, where the radiative loss exceeds the incident solar irradiance (as shown in Fig. 1a) [22]. Design and fabrication of near-ideal selective solar absorbers are challenging to achieve high temperatures under one sun (1 kW/m^2) solar irradiance. For example, the solar absorber cannot be heated above a temperature at which incident energy will be equal to radiation losses under one sun for a given average emissivity. With the increase in operating temperature,

* Corresponding author.
** Corresponding author.
E-mail addresses: boevyzbw@163.com (B. Zhang), chamolisandeep28@gmail.com (S.K. Chamoli).

https://doi.org/10.1016/j.solmat.2023.112383
Received 1 March 2023; Received in revised form 29 April 2023; Accepted 12 May 2023
Available online 31 May 2023

the transition wavelength shifts towards a shorter wavelength due to a larger overlap of the BB radiation curve with the solar spectrum. Additionally, the absorber should have thermally, mechanically, and chemically stable at operating temperature. For example; metals used in a cermet-based absorber get oxidized at high temperatures, thus they require an environmental barrier layer to protect the metal [23,24]. Several broadband solar absorbers are proposed based on lattice-scattering effects, excitation of slow-light modes, impedance matching, multiple resonances, and adiabatic nano-focusing of gap surface plasmon modes and multilayer thin film [22,25–40]. Most of the previous designs need intense lithography to prepare the top anti-reflective layer which increases the cost of the solar absorber.

In this paper, we theoretically and experimentally design a near-ideal selective solar absorber made of a dielectric-metal-dielectric-metal (DMDM) structure. We chose transition metals such as chromium (Cr), titanium (Ti), and tungsten (W) due to their earth abundance, large melting point, and mechanical and chemical stability at high temperatures. Aluminum dioxide (Al_2O_3) is chosen as the dielectric material. First, we compare the average absorption or emission response of all three metals in the DMDM configuration. We realized that the design with tungsten as the metal layer has maximum absorption response along minimum emission for blackbody working 600 K and closest spectral matching to an ideal selective solar absorber. Moreover, a high melting point with a low thermal expansion coefficient of W makes it the best material choice for high-temperature applications and it shows good stability at 800 K [41]. The top dielectric layer acts as a protective layer and assists optical absorption in the broadband spectral region [42,43]. Our simulation results agree well with previous experimental work on a similar design [44]. Using simulated spectral absorbance/emittance of the designed solar absorbers, we calculated corresponding steady-state temperatures under one sun (1 kW/m^2) solar irradiance with normal and forced convection losses. Due to ideal selective absorption and emission, the design made of W has shown the best steady-state temperature of ~100 K. Furthermore, we fabricated an absorber with W as a metal and found that it increases temperature by ~100 K when exposed to the sun. The calculated steady-state temperature is in good agreement with this result.

2. Proposed approach and design

An ideally selective absorber has two spectral regions. The first, shorter wavelength, region needs to have the unit (100%) absorbance/emittance while the second, longer wavelength, region requires zero absorbance/emittance. Both regions are separated by a sharp transition wavelength (λ_C). Transition wavelength is the wavelength where radiation loss exceeds the incident solar irradiance. Fig. 1a shows BB radiation curves at 400 K, 600 K, 800 K, and 1000 K temperatures and corresponding λ_C values at 2.42 μm, 1.8 μm, 1.13 μm, and 1.11 μm wavelengths. The transition wavelength shifts towards a shorter wavelength with a larger overlap between solar irradiance and BB radiation curve as operating temperature increases. It is noticeable that λ_C is not a smooth function of temperature because solar irradiance is not a smooth spectrum and λ_C can not be seen in a region where solar irradiance is zero due to atmospheric absorption. The blackbody curve is drawn using: $I_{BB}(T,\lambda) = \frac{2hc^2}{\lambda^5}\frac{1}{e^{hc/\lambda k_B T}-1}$, where h is the Plank's constant, c is the speed of light, k_B is the Boltzmann constant, and λ is the wavelength. Due to the broadband nature of Planck's radiation law, it's beneficial to have low absorption for all the wavelengths which is not contributing significantly to solar radiation absorption. So, such a low absorption in the range of 3–7.5 μm shown by DMDM structure has the potential to be used in TPV technology. The ideal absorber should cover most of the

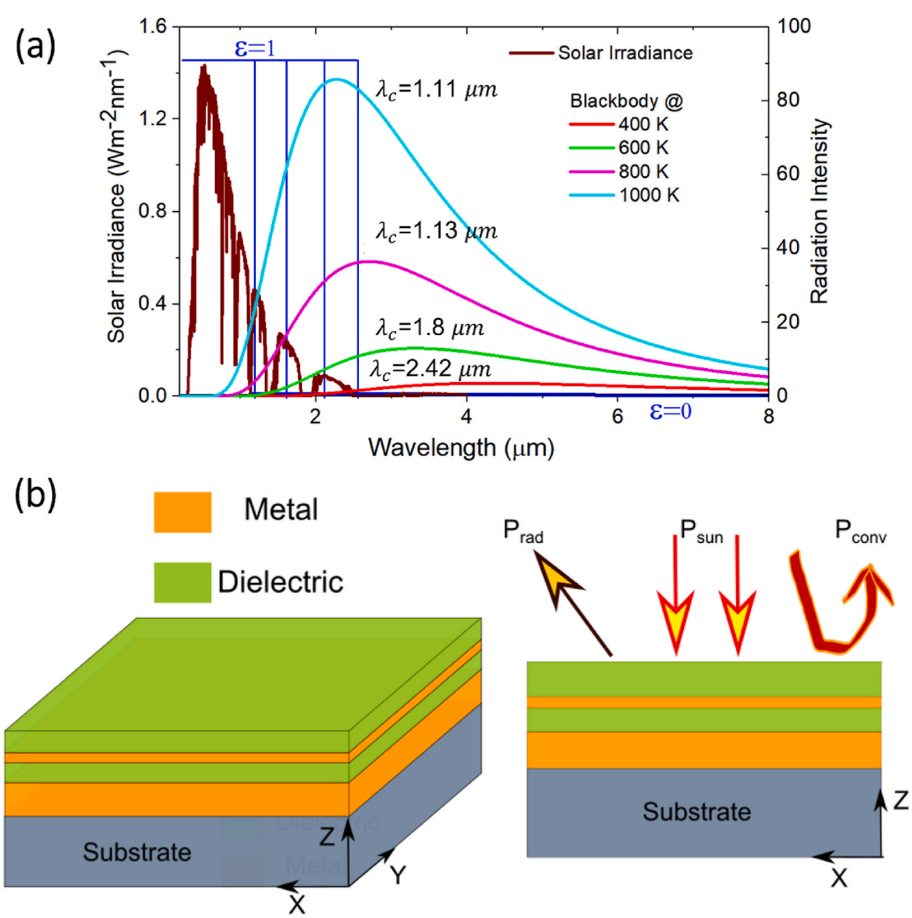

Fig. 1. **(a)** Unconcentrated AM 1.5G direct (brown color, left axes) solar irradiance and blackbody radiation spectrum (right axes) at 400 K (red color), 600 K (green color), 800 K (pink color) and 1000 K (cyan color). The ideal emittance (ε) profile (blue curve), a step function with sharp transitions from 1 to 0 represents a transition wavelength (λ_C) where the ideal emittance profile at a given temperature cut the solar irradiance curve, for example λ_C is 2.42 μm, 1.81 μm, 1.13 μm and 1.11 μm at 400 K, 600 K, 800 K, and 1000 K. **(b)** Schematic of proposed DMDM structure for high-temperature application. The metal layer is made of three transition metals Cr, Ti, and W, Al_2O_3 is a dielectric layer.

electromagnetic window from ultraviolet (UV), visible to near-infrared (NIR) as shown in Fig. 1.

A schematic of the proposed multilayer metal insulator broadband absorber is shown in Fig. 1b. The structure has four layers on the glass substrate in an alternate metal-dielectric fashion. The top dielectric layer works as an environmental protective layer as well as an antireflection layer to increase the absorption of the proposed metal-dielectric metal (MDM) resonator. In the MDM cavity, the bottom metal layer is thick (~100 nm) enough to suppress the transmission, the top metal is semitransparent (~12 nm), and Al_2O_3 is a lossless dielectric spacer between two metal layers. Therefore, the DMDM configuration forms an asymmetric Fabry-Perot (FP) resonator [45]. The absorption is calculated using $A + R + T = 1$, where A is absorption, R is reflection and T is transmission. T is zero because the thickness of bottom metal is more than 100 nm. So, the A = 1-R. We have proposed three DMDM using three different transition metals: Cr, Ti, and W, (i) Al_2O_3-Cr-Al_2O_3-Cr, (ii) Al_2O_3-Ti-Al_2O_3-Ti and (iii) Al_2O_3-W-Al_2O_3–W. The top Al_2O_3 layer works as a protective and AR coating layer and increases the overall absorption of structure. As resonance strongly depends on the incident wavelength and thickness of the middle insulator layer, therefore we optimized the thicknesses of all proposed absorbers and calculated as [46]: t_t (thickness of the top metal layer) = 14 nm, t_b (thickness of the bottom metal layer) = 100, optically thick to suppress the transmission, d_t (thickness of the top dielectric layer) = 80 nm and d_b (thickness of the bottom dielectric layer) = 200 nm.

3. Results and discussions

3.1. Theoretical background

Fig. 2 a, c, and **e** demonstrate color-coded spectral absorptance as a function of incidence angle and wavelength for all three designed selective solar absorber systems *Cr*, *Ti*, and *W*, respectively. The resonance absorption is strong, and close to unity, even at higher angles for all three absorbers. In all three cases, the absorption is polarization independent and omnidirectional. Fig. 2 b, d, and **f** show the absorption at normal incidence for all three absorbers and the available solar irradiance curve (AM1.5G) for each wavelength. For normal incidence cases, *W* provides the best absorption with near perfect in the range of 500–800 nm and closely follows the solar spectral curve (Fig. 2f). Red dark circles in Fig. 2 (b, d, and f) represent λ_C for different operating temperatures, taken from Fig. 1a. The green box represents the ideal emissivity curve at 600 K and the crossing solar irradiance curve at λ_C = 1.81 μm. So ideally, before λ_C = 1.81 μm emissivities should be 1 and after λ_C = 1.81 μm should be 0.

As the bottom layer is optically thick enough to suppress the transmission and the top layer must be optically thin to allow incident light coupled into the MDM cavity. The refractive index of the dielectric spacer between the thick and thin metal layers is an important parameter in determining the resonance wavelength of the cavity mode. Therefore, we optimized the thickness of each layer to achieve the required ideal absorption using the transfer matrix method (TMM) in finite-difference time-domain (FDTD). The transmitted light from the

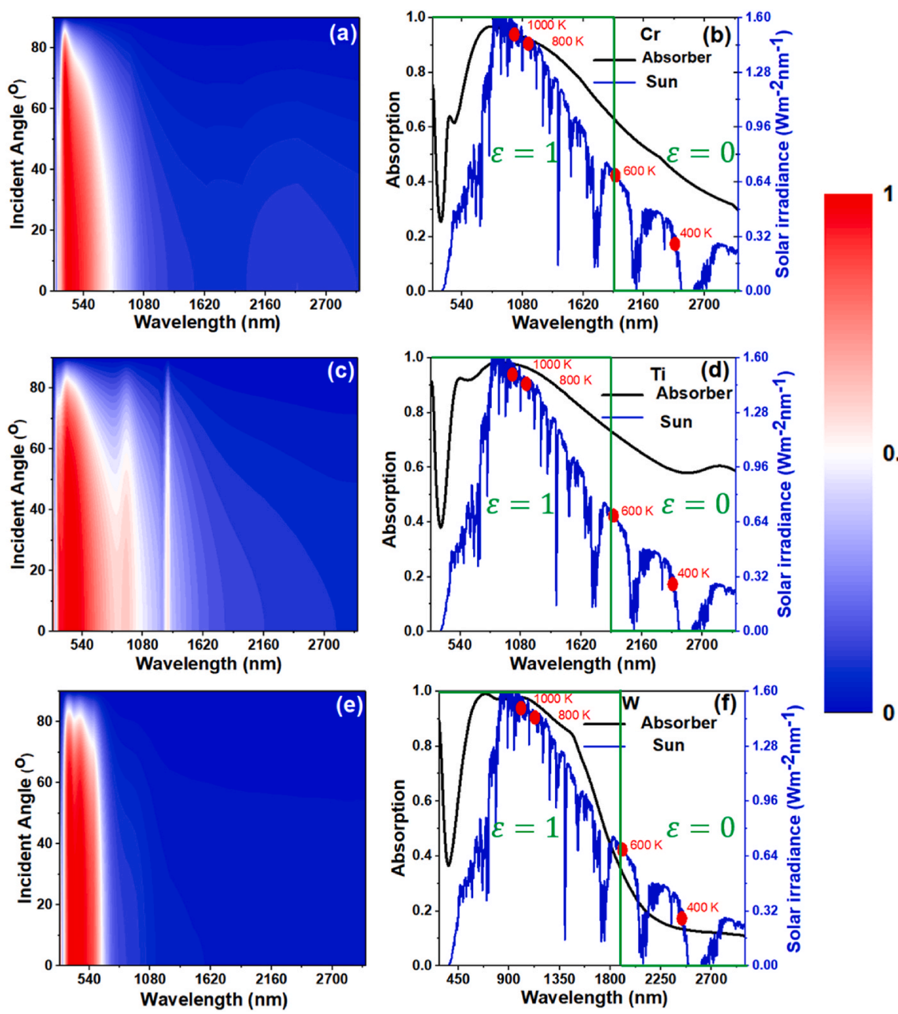

Fig. 2. Absorption as a function of incident angle and wavelength for *Cr*, *Ti*, and *W* as a metal in DMDM configuration **(a), (c),** and **(e)**, respectively. Absorption (left) at the normal incident and available solar irradiance (right) in the wavelength range of interest for Cr, Ti, and W in **(b), (d)** for **(f)** respectively. Red-filled circles in (b), (d), and (f) are representing the transition wavelength for a blackbody at 400 K, 600 K, 800 K, and 1000 K, taken from Fig. 2. The green line represents an ideal emissivity step function at 600 K temperature. Using the following parameters: t_t = 14 nm and t_b= 50 nm, d_t = 100 nm, and d_b= 80 nm.

top thin metal coupled into the cavity and trapped inside it with continuous back and forth reflection. In each reflection, the light gets absorbed and finally gets completely absorbed. The origin of the resonance peak at a lower wavelength can be understood by MDM FP nanocavity and can be given by equation (1) [46,47].

$$2\left(\frac{2\pi}{\lambda_{res}}\right)n_i d_i + \Psi_b + \Psi_t = 2\pi m \quad (1)$$

Where λ_{res} represents resonance wavelength, n is the refractive index of the dielectric layer and d is the thickness of the middle insulator layer in the MDM structure. m is the mode order. Ψ_b and Ψ_t are the phase change due to the top and bottom metal layers, respectively.

Next, we calculate the average emissivity/absorptivity of an absorber working at 600 K with respect to the emission angle in the solar (below λ_C for 600 K) and non-solar (above λ_C for 600 K) window. Average absorptivity $\overline{\alpha}$ and emissivity $\overline{\varepsilon}$ are calculated using the following expression [48]:

$$\overline{\alpha} = \int_{0.28\mu m}^{1.81\mu m} \alpha(\lambda).I_{AM1.5}(\lambda)d\lambda \Big/ \int_{0.28\mu m}^{1.81\mu m} I_{AM1.5}(\lambda)d\lambda \quad (2)$$

$$\overline{\varepsilon}\,(T) = \int_{1.81\mu m}^{4\ \mu m} \varepsilon(\lambda).I_{AM1.5}(\lambda)d\lambda \Big/ \int_{1.81\mu m}^{4\mu m} I_{BB}(\lambda, T)d\lambda \quad (3)$$

Where $I_{AM1.5}(\lambda)$ and $I_{BB}(\lambda)$ are solar irradiance and blackbody spectrum at a given wavelength and temperature. According to Kirchoff's law of thermal radiation at thermal equilibrium absorptivity α_λ must be equal to emissivity, due to reciprocity ε_λ $[\alpha_\lambda = \varepsilon_\lambda]$ [20]. Fig. 3 **(a)** and **(b)** represent average emissivity as a function of emission angle θ in the wavelength range of 0.28 μm–1.81 μm and 1.81 μm–4 μm. All three absorbers are having high average absorption (>86%) in the angular range of 0° to 60° and from 60° to 80° absorption is >70%. The absorber made of *W* as a metal demonstrates the best absorption in the entire angular range. At the same time absorber made of *W* shows average emissivity of <10% in the spectral window outside the λ_C in the entire angular range. Absorber made of *Ti* shows average emissivity of >40% and *Cr* shows >60%. Due to high average emissivity below λ_C and low average emissivity above λ_C, absorber made of *W* is best choice and used as a metal layer in our further calculations related to steady state temperature in this paper.

Table 1 (in Supplementary Information) shows the average absorptance ($\overline{\alpha}$) and emittance ($\overline{\varepsilon}$) at a given temperature for a few previously proposed selective solar absorbers made of thin film multilayer [38,49–52], Photonics Crystal [53–55], cermet based [56,57], and metamaterial [58,59]. Out of all absorbers, cermet-based absorbers have witnessed great commercial success. However, absorbers based on photonics crystal and multilayer stacks made of metal, dielectric, and semiconductor have shown significant performance improvement for ideal selective absorbers as we can control the absorption and emission response of absorber according to cut-off wavelength λ_C [20]. Proposed metal dielectric design shows near ideal absorption and emission for an absorber working at 600 K. Note that in our calculations we considered natural (h = 5.7 W/m^{2}K) and forced (h = 20 W/m^{2}K) convective heat losses. However, previous papers do not discuss about the convective losses and its effect on performance.

Fig. 4 shows electric field intensity as a function of incident wavelength and absorber depth along the light propagation (Z) direction for all three designed absorbers. Comparatively low-field confinement in the middle Al_2O_3 layer confirms a low-quality factor of the cavity. Most of the incident light is absorbed by the top metal layer and the bottom metal acts as a mirror with less dissipation of power. The electric field is strongly get confined between the absorptive metal layer and the top Al_2O_3 layer. As the permittivity of the metal is larger than the Al_2O_3, it is also evident that the electric field distributed in the top Al_2O_3 layer is significant not only at the resonance but also for the entire solar spectra region. At a longer wavelength, the effective thickness of the metal is less, therefore it does not affect the EM field propagation until it reaches the bottom metal layer and gets reflected. The power absorbed from the structure is proportional to the electric field intensity $|E|^2$ and can be expressed as: $P_{abs} = \frac{1}{2}\omega\varepsilon_0 nk|E|^2$. Where ω and ε_0 are angular frequency and permittivity of free space, n and k are real and imaginary parts of the refractive index. In a DMDM absorber, the top insulator layer helps to couple the light into the MDM cavity by reducing the reflection through the reduction in the index mismatch at the air-solid interface. After the AR coating layer, the light gets partially absorbed in the metal layer and ultimately coupled critically into the MDM cavity through multiple back-and-forth reflections. As the light intensity is reduced from the first thin metal film, therefore it cannot pass through the thick back metal reflector and get reflected into the air. It's evident from Fig. 4d most of the light is absorbed in the top metal and a bit in the bottom metal layer.

3.2. Steady state temperature calculation

Next, we study the power balance in the absorber and calculate the steady-state temperature, using the following expressions [60]:

$$P_{out}(T) = P_{sun} - P_{rad} - P_{para} \quad (4)$$

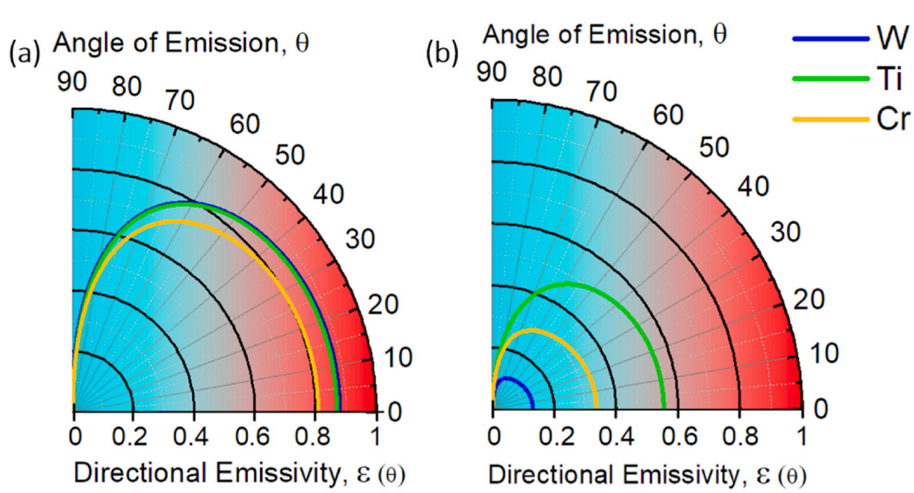

Fig. 3. Average emissivity $\overline{\varepsilon}$ as a function of emission angle for an emitter working at 600 K i.e. λ_C = 1.81 μm **(a)** $\overline{\varepsilon}$ for wavelength ranging from 0.28 μm to 1.81 μm and **(b)** $\overline{\varepsilon}$ in the wavelength from 1.81 μm to 4 μm.

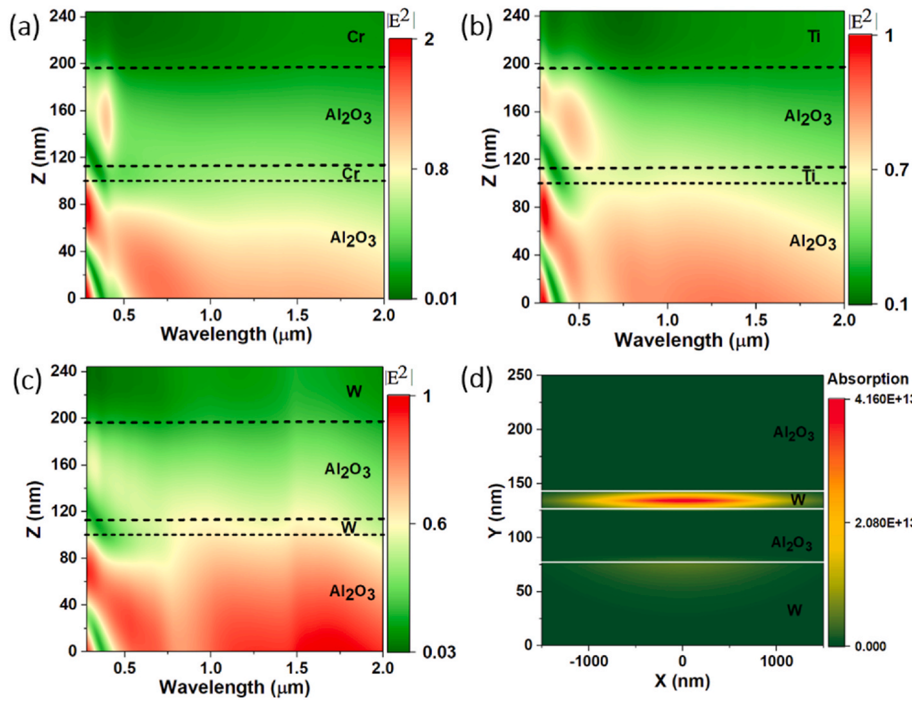

Fig. 4. Electric field intensity distribution in depth direction Z for an absorber made of (a) Cr, (b) Ti, (c) W, and (d) power absorbed in the absorber in case of W. Using the following parameters: $t_t = 14$ nm and $t_b = 50$ nm $d_t = 100$ nm and $d_b = 80$ nm.

Where $P_{out}(T)$ is the useable solar-thermal power as output from the structure, P_{sun} is solar power absorbed by the structure from the sun, and P_{rad} and P_{para} are radiation and parasitic losses from the structure. The power absorber by the structure from sun, P_{sun} is given as $P_{sun} = A\int_0^\infty d\lambda \varepsilon_{abs}(\lambda, \theta_{sun}) I_{AM1.5}(\lambda)$. Where A is the absorber's surface area ε_{abs} is spectral emittance/absorbance of the absorber at a given wavelength and incident angle or sun angle. The power radiated by the structure is given by: $P_{rad}(T) = A\int d\Omega \cos\theta \int_0^\infty d\lambda I_{BB}(T, \lambda)\varepsilon(\lambda, \theta)$, $\int d\Omega = 2\pi\int_0^{\frac{\pi}{2}} d\theta \sin\theta$, represents angular integral over a hemisphere. Solar irradiance $I_{AM1.5}$ is used as shown in Fig. 2. The emissivity of the absorber is equal to the absorption due to Kirchhoff's law of reciprocity. The absorption of all three absorbers are taken from Fig. 2. $I_{BB}(T, \lambda)$ is blackbody spectral radiance at a given temperature T and wavelength λ. In our calculations, we consider the stringent condition of heat loss convectively. The convective transfer coefficient h primarily depends on the wind velocity V_{wind}. It is generally categorized as forced or assisted and free or natural convection. Heat transfer is related to wind velocity V_{wind} by $h = 5.7 + 3.8\ V_{wind}$. Heat transfer is linearly related to the wind velocity as shown in Fig. 5a. Convective heat loss can be simply calculated using the expression: $P_{conv} = h\,A\,\Delta T$, where A is the surface area of the absorber and ΔT is the temperature difference between the ambiance and absorber. Fig. 5b shows the convective heat lost as a function of h for different ΔT, we can strong enhancement in the heat loss due to high ΔT. For forced and free convection, the typical values for h are as follows: Free Convection - air, gases, and dry vapors: 0.5–1000 (W/(m^2K)), Forced Convection - air, gases, and dry vapors: 10–1000 (W/(m^2K)) [48]. Now using the expression for P_{sun}, P_{rad} and P_{conv}, one can find out the steady state temperature using power balance equation at which the net power output from the absorber is zero, i.e., $P_{out}(T) = 0$.

To calculate the steady-state temperature, we keep the ambiance temperature T_{amb} equal to 300 K and keep on increasing the temperature of the absorber T (starting from 300 K) until the net power, $P_{out}(T) = 0$. Further increase in the absorber temperature over the steady state temperature will have higher losses than the incident solar power

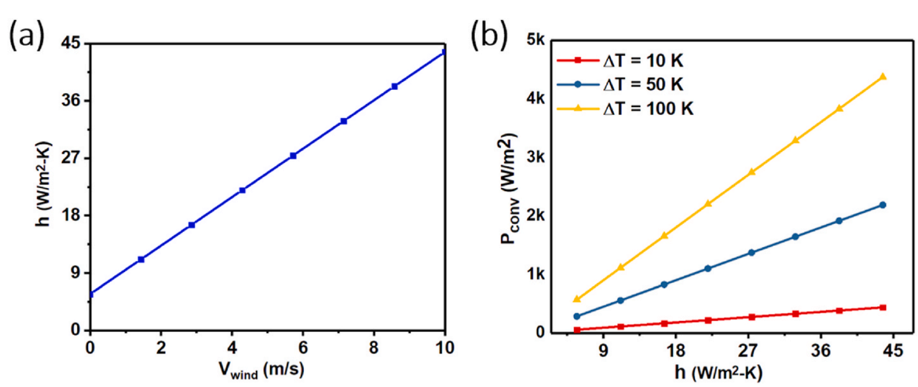

Fig. 5. **(a)** Heat lost coefficient and wind velocity, **(b)** Heat loss convectively P_{conv} versus heat loss coefficient.

resulting in negative P_{out}. The negative P_{out} means the power is flowing from the absorber to the ambient. The black dashed line (Fig. 6) corresponds to the steady state temperature and sun angle pairs where the net power is 0. It shows power out at three different *h* values for all three solar absorbers. As expected, the *h* value significantly affects the solar-thermal power output from the absorbers and its temperature rise ($\Delta T = T\text{-}T_{amb}$). For all the absorbers and *h* values, the ΔT value is maximum and constant in an angular range from normal to ~70° oblique incidence. This shows that the absorbers can be used in a flat plane, without tracking, from morning to evening with constant performance. We can see that ΔT is maximum for *W* when $h = 0$, but as *h* increases ΔT reduces due to higher parasitic losses.

3.3. Experimental realization

Fig. 7a shows a cross-sectional scanning electron microscope image of the DMDM design with *W* on silicon. Direct current (DC) and radio frequency (RF) Sputtering methods are used to fabricate the sample. Metal DC and dielectric RF sputtering have been used. It is possible to deposit both metal and dielectric in one chamber showing that such a method is cost-effective. The thickness of each of the layers matches the design proposed. We then measured average angular absorption which is well in agreement with the simulation as shown in Fig. 7b.

An example of a measurement setup is shown in Fig. 7c, which shows a solar simulator is used to heat the sample under one sun condition. Using low thermal conductivity white polystyrene, the customized measurement chamber is mounted on a whiteboard, which is covered with aluminum tape to prevent solar heating. To minimize thermal interaction between samples and the sample cradle, white polystyrene is used as the sample cradle. For measuring the temperature of the sample, a thermocouple is attached to the front side. Convection is minimized by covering the chamber with low-density polyethylene film after the sample set. The thermocouple measures temperature on the sample surface as a function of time in Fig. 7d. The calculated steady-state temperature for the *W* sample is nearly the same as the steady-state temperature calculated for the steady-state temperature of the *W* sample at 100 K. Discrepancies are expected, however, due to variations in thickness and refractive index during fabrication. A heat transfer coefficient is also expected to cause the discrepancy. The emissivity of the sample in the 8–12 μm range is also calculated using a thermal camera, which results in about 5% emissivity in the IR range (8–12 *m*) (see the Supplementary Fig. 1).

4. Conclusion

In conclusion, we have designed and demonstrated a lithographic fee broadband ideal selective solar absorber for high-temperature applications. We proposed three absorbers made of transition metals: *Cr*, *Ti*, and

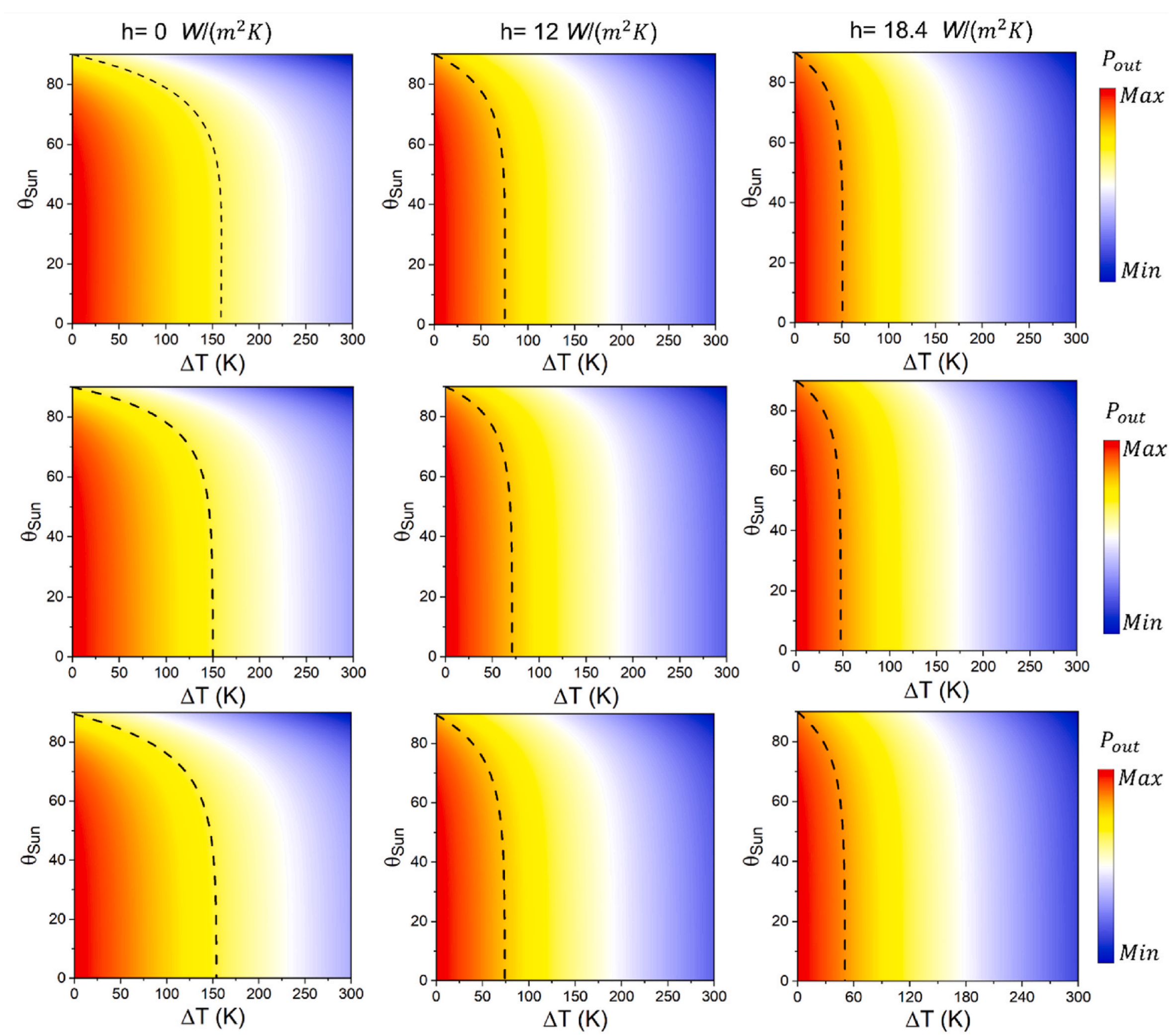

Fig. 6. Steady-state temperature calculation: Steady-state temperature calculation and power out for proposed absorbers as a function of sun angle (θ_{sun}) and temperature difference ΔT (T -T_{amb}). The Black dotted line traces out the steady-state temperature for all three absorbers at h= 5.7 W/m^{2}K, h= 12 W/m^{2}K, and h= 18.4 W/m^{2}K. (a), (b) and (c) for W: (d), (e), and (f) for Cr: (g), (h), and (i) for Ti.

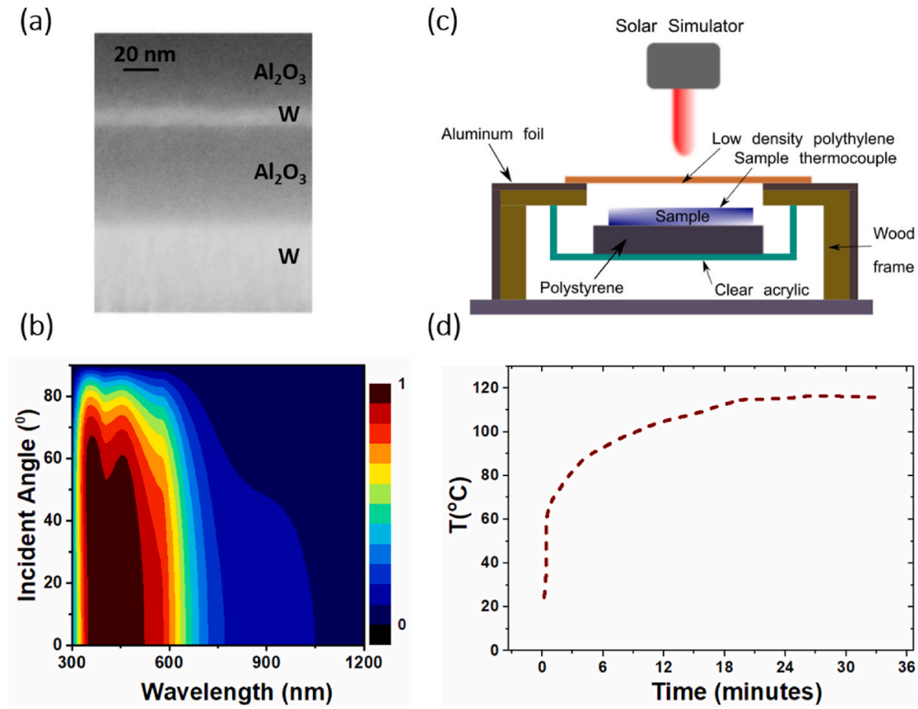

Fig. 7. Experimental realization: (a) SEM image of fabricated DMDM design with W. (b) Measured absorption as a function of wavelength and angle. (c) Schematic of the measurement chamber. (d) Measured steady state temperature.

W. All absorbers showed polarization-independent and omnidirectional absorption. We analyzed the absorption in all three cases and compare it to an ideal. The absorption spectra for *W* at 600 K are very close to ideal. We calculated the steady-state temperature of the absorber using the power balance equation. In the end, we fabricated *W*-based absorbers and measured the temperature rise experimentally. Following that, we measured the absorption as a function of wavelength and angle. The proposed absorber has a broadband response to 80° with high absorption, insensitivity to incident light polarization, and lithographic-free design with cheap materials, which makes it an ideal candidate for high-temperature applications. Finally, we measured a steady state temperature of 100 K, which was in good agreement with the calculated Solar TPV systems, solar thermal energy conversion, and TPV systems can all benefit from the proposed design. steady state temperature.

Funding

The work is Supported by Research on interference optimization of cellular networks based on intelligent reflecting surface project of science and technology research program of Chongqing Education Commission of China (No. KJQN202203101).

CRediT authorship contribution statement

Bowei Zhang: Formal analysis, Data curation. **Sandeep Kumar Chamoli:** Conceptualization.

Declaration of competing interest

The authors declare that they have no known competing financial interests or personal relationships that could have appeared to influence the work reported in this paper.

Data availability

Data will be made available on request.

Nomenclature

TPV	Thermo photovoltaic
PV	Photovoltaic
BB	Blackbody radiation
MDM	Metal-Dielectric-Metal
TMM	Transfer Matrix Method
FDTD	Finite-Difference Time-Domain
FP	Fabry-Perot
DMDM	Dielectric-Metal-Dielectric-Metal
DC	Direct Current
RF	Radio Frequency
$\overline{\alpha}$	Absorptance
$\overline{\varepsilon}$	Emittance
P_{out}	Power as output from the structure
P_{rad}	Radiation Losses

P_{para} Parasitic Losses
P_{sun} Solar power absorbed by the structure from the sun
I_{BB} Blackbody spectral radiance
V_{wind} Wind velocity
θ_{sun} Sun Angle

Appendix A. Supplementary data

Supplementary data to this article can be found online at https://doi.org/10.1016/j.solmat.2023.112383.

References

[1] N. Selvakumar, H.C. Barshilia, Review of physical vapor deposited (PVD) spectrally selective coatings for mid- and high-temperature solar thermal applications, Sol. Energy Mater. Sol. Cells 98 (2012) 1–23, https://doi.org/10.1016/j.solmat.2011.10.028.
[2] G. Huang, K. Wang, C.N. Markides, Efficiency limits of concentrating spectral-splitting hybrid photovoltaic-thermal (PV-T) solar collectors and systems, Light Sci. Appl. (2021) 1–14, https://doi.org/10.1038/s41377-021-00465-1.
[3] K. Gu, H. Zhong, A general methodology to measure the light-to-heat conversion efficiency of solid materials, Light Sci. Appl. 12 (2023) 120, https://doi.org/10.1038/s41377-023-01167-6.
[4] S.A. Jalil, M. ElKabbash, Zihao li, J. Zhang, S. Singh, Z. Zhan, C. Guo, Multipronged heat-exchanger based on femtosecond laser-nano/microstructured Aluminum for thermoelectric heat scavengers, Nano Energy 75 (2020), 104987, https://doi.org/10.1016/j.nanoen.2020.104987.
[5] Z. Zhan, M. Elkabbash, Z. Li, X. Li, J. Zhang, J. Rutledge, S. Singh, C. Guo, Nano Energy Enhancing thermoelectric output power via radiative cooling with nanoporous alumina, Nano Energy 65 (2019), 104060, https://doi.org/10.1016/j.nanoen.2019.104060.
[6] S.A. Jalil, B. Lai, M. Elkabbash, Spectral absorption control of femtosecond laser-treated metals and application in solar-thermal devices, Light Sci. Appl. (2020), https://doi.org/10.1038/s41377-020-0242-y.
[7] C. Fei Guo, T. Sun, F. Cao, et al., Metallic nanostructures for light trapping in energy-harvesting devices, Light Sci. Appl 3 (2014) e161, https://doi.org/10.1038/lsa.2014.42.
[8] K. Millien, Prototype steam turbine for solar power production, Adv. Mater. Sci. Eng. 2020 (2020), https://doi.org/10.1155/2020/4589281.
[9] P.A. Davies, A. Luque, Solar thermophotovoltaics: brief review and a new look, Sol. Energy Mater. Sol. Cells 33 (1994) 11–22, https://doi.org/10.1016/0927-0248(94)90284-4.
[10] YB. Kim, JW. Cho, YJ. Lee, et al., High-index-contrast photonic structures: a versatile platform for photon manipulation, Light Sci. Appl. 11 (2022) 316, https://doi.org/10.1038/s41377-022-01021-1.
[11] S.C. Singh, M. ElKabbash, Z. Li, X. Li, B. Regmi, M. Madsen, S.A. Jalil, Z. Zhan, J. Zhang, C. Guo, Superwicking black metal surface for solar-thermal water sanitation, Opt Photon. News 31 (2020) 60, https://doi.org/10.1364/opn.31.12.000060.
[12] C. Xi, Y. Hongxing, L. Lin, W. Jinggang, L. Wei, Experimental studies on a ground coupled heat pump with solar thermal collectors for space heating, Energy 36 (2011) 5292–5300, https://doi.org/10.1016/j.energy.2011.06.037.
[13] Y. Tian, C.Y. Zhao, A review of solar collectors and thermal energy storage in solar thermal applications, Appl. Energy 104 (2013) 538–553, https://doi.org/10.1016/j.apenergy.2012.11.051.
[14] H. Dong, C. Ran, W. Gao, et al., Metal Halide Perovskite for next-generation optoelectronics: progresses and prospects, eLight 3 (2023) 3, https://doi.org/10.1186/s43593-022-00033-z.
[15] SJ. Lee, HC. Cheng, Y. Wang, et al., Lead halide perovskite sensitized WSe_2 photodiodes with ultrahigh open circuit voltages, eLight 3 (2023) 8, https://doi.org/10.1186/s43593-023-00040-8.
[16] A. Lenert, D.M. Bierman, Y. Nam, W.R. Chan, I. Celanović, M. Soljačić, E.N. Wang, A nanophotonic solar thermophotovoltaic device, Nat. Nanotechnol. 9 (2014) 126–130, https://doi.org/10.1038/nnano.2013.286.
[17] I.E. Khodasevych, L. Wang, A. Mitchell, G. Rosengarten, Micro- and nanostructured surfaces for selective solar absorption, Adv. Opt. Mater. 3 (2015) 852–881, https://doi.org/10.1002/adom.201500063.
[18] E. Rephaeli, S. Fan, Absorber and emitter for solar thermo- photovoltaic systems to achieve efficiency exceeding the Shockley-Queisser limit, Opt Express 17 (2009) 1421–1424.
[19] R. Taylor, T. Otanicar, G. Rosengarten, Nanofluid-based optical filter optimization for PV/T systems, Light Sci. Appl. 1 (2012) e34, https://doi.org/10.1038/lsa.2012.34.
[20] L.A. Weinstein, J. Loomis, B. Bhatia, D.M. Bierman, E.N. Wang, G. Chen, Concentrating solar power, Chem. Rev. 115 (2015) 12797–12838, https://doi.org/10.1021/acs.chemrev.5b00397.
[21] H. Zhu, Q. Li, C. Zheng, et al., High-temperature infrared camouflage with efficient thermal management, Light Sci. Appl. 9 (2020) 60, https://doi.org/10.1038/s41377-020-0300-5.
[22] Z.M. Zhang, Nano/microscale Heat Transfer, McGraw-Hill, New York, 2007.
[23] J. Gao, C. Tu, L. Liang, H. Zhang, F. Zhuge, L. Wu, H. Cao, K. Yu, Silver nanoparticles with an armor layer embedded in the alumina matrix to form nanocermet thin films with sound thermal stability, ACS Appl. Mater. Interfaces 6 (2014) 11550–11557, https://doi.org/10.1021/am502254s.
[24] G. Baraldi, M. Carrada, J. Toudert, F.J. Ferrer, A. Arbouet, V. Paillard, J. Gonzalo, Preventing the degradation of Ag nanoparticles using an ultrathin a-Al 2O3 layer as protective barrier, J. Phys. Chem. C 117 (2013) 9431–9439, https://doi.org/10.1021/jp401421m.
[25] F. Ding, L. Mo, Ultra-broad flat band light absorber based on multisized slow-wave hyperbolic metamaterial thin-films, CLEO QELS - Fundam. Sci. CLEO_QELS 147 (2015) 1551, https://doi.org/10.1364/CLEO_AT.2015.JTu5A.102, 2015.
[26] T.A. Cooper, S.H. Zandavi, G.W. Ni, Y. Tsurimaki, Y. Huang, S.V. Boriskina, G. Chen, Contactless steam generation and superheating under one sun illumination, Nat. Commun. 9 (2018) 1–10, https://doi.org/10.1038/s41467-018-07494-2.
[27] S.K. Chamoli, S.C. Singh, C. Guo, 1-D metal-dielectric-metal grating structure as an ultra-narrowband perfect plasmonic absorber in the visible and its application in glucose detection, Plasmonics 15 (2020) 1339–1350, https://doi.org/10.1007/s11468-020-01161-3.
[28] Q. Lin, Z. Wang, M. Young, J.B. Patel, R.L. Milot, L. Martinez Maestro, R.R. Lunt, H. J. Snaith, M.B. Johnston, L.M. Herz, Near-infrared and short-wavelength infrared photodiodes based on dye–perovskite composites, Adv. Funct. Mater. 27 (2017) 1–7, https://doi.org/10.1002/adfm.201702485.
[29] Y. Cui, K.H. Fung, J. Xu, H. Ma, Y. Jin, S. He, N.X. Fang, Ultrabroadband light absorption by a sawtooth anisotropic metamaterial slab, Nano Lett. 12 (2012) 1443–1447, https://doi.org/10.1021/nl204118h.
[30] P. Zhu, L. Jay Guo, High performance broadband absorber in the visible band by engineered dispersion and geometry of a metal-dielectric-metal stack, Appl. Phys. Lett. 101 (2012) 1–4, https://doi.org/10.1063/1.4771994.
[31] A. Al-Rjoub, L. Rebouta, P. Costa, N.P. Barradas, E. Alves, P.J. Ferreira, K. Abderrafi, A. Matilainen, K. Pischow, A design of selective solar absorber for high temperature applications, Sol. Energy 172 (2018) 177–183, https://doi.org/10.1016/j.solener.2018.04.052.
[32] H. Deng, Z. Li, L. Stan, D. Rosenmann, D. Czaplewski, J. Gao, X. Yang, Broadband perfect absorber based on one ultrathin layer of refractory metal, Opt. Lett. 40 (2015) 2592, https://doi.org/10.1364/ol.40.002592.
[33] F. Ding, Y. Jin, B. Li, H. Cheng, L. Mo, S. He, Ultrabroadband strong light absorption based on thin multilayered metamaterials, Laser Photon. Rev. 8 (2014) 946–953, https://doi.org/10.1002/lpor.201400157.
[34] V. Steenhoff, M. Theuring, M. Vehse, K. von Maydell, C. Agert, Ultrathin resonant-cavity-enhanced solar cells with amorphous germanium absorbers, Adv. Opt. Mater. 3 (2015) 182–186, https://doi.org/10.1002/adom.201400386.
[35] M.C. Soydan, A. Ghobadi, D.U. Yildirim, V.B. Erturk, E. Ozbay, All ceramic-based metal-free ultra-broadband perfect absorber, Plasmonics 14 (2019) 1801–1815, https://doi.org/10.1007/s11468-019-00976-z.
[36] T. Søndergaard, S.M. Novikov, T. Holmgaard, R.L. Eriksen, J. Beermann, Z. Han, K. Pedersen, S.I. Bozhevolnyi, Plasmonic black gold by adiabatic nanofocusing and absorption of light in ultra-sharp convex grooves, Nat. Commun. 3 (2012) 1–6, https://doi.org/10.1038/ncomms1976.
[37] Yu Zhou, Zheng Qin, Zhongzhu Liang, Meng Dejia, Haiyang Xu, David R. Smith, Yichun Liu, Ultra-broadband metamaterial absorbers from long to very long infrared regime, Light Sci. Appl 10 (2021) 138, https://doi.org/10.1038/s41377-021-00577-8.
[38] N.H. Thomas, Z. Chen, S. Fan, A.J. Minnich, Semiconductor-based multilayer selective solar absorber for unconcentrated solar thermal energy conversion, Sci. Rep. 7 (2017) 3–8, https://doi.org/10.1038/s41598-017-05235-x.
[39] L. Wen, Z. Sun, Q. Zheng, et al., On-chip ultrasensitive and rapid hydrogen sensing based on plasmon-induced hot electron–molecule interaction, Light Sci. Appl. 12 (2023) 76, https://doi.org/10.1038/s41377-023-01123-4.
[40] L. Zhu, F. Liu, H. Lin, et al., Angle-selective perfect absorption with two-dimensional materials, Light Sci. Appl. 5 (2016), e16052, https://doi.org/10.1038/lsa.2016.52.
[41] E. Rephaeli, S. Fan, Tungsten black absorber for solar light with wide angular operation range, Appl. Phys. Lett. 92 (2008) 8–10, https://doi.org/10.1063/1.2936997.
[42] N.I. Landy, S. Sajuyigbe, J.J. Mock, D.R. Smith, W.J. Padilla, Perfect metamaterial absorber, Phys. Rev. Lett. 100 (2008) 1–4, https://doi.org/10.1103/PhysRevLett.100.207402.
[43] Z.J. Coppens, I.I. Kravchenko, J.G. Valentine, Lithography-free large-area metamaterials for stable thermophotovoltaic energy conversion, Adv. Opt. Mater. 4 (2016) 671–676, https://doi.org/10.1002/adom.201500727.
[44] M. Chirumamilla, A.S. Roberts, F. Ding, D. Wang, P.K. Kristensen, S.I. Bozhevolnyi, K. Pedersen, Multilayer tungsten-alumina-based broadband light absorbers for

high-temperature applications, Opt. Mater. Express 6 (2016) 2704, https://doi.org/10.1364/ome.6.002704.

[45] A. Phys, Ultra-narrow-band light dissipation by a stack of lamellar silver and alumina, Appl. Phys. Lett. 104 (104) (2017), 221107, https://doi.org/10.1063/1.4881267.

[46] S.K. Chamoli, G. Verma, S.C. Singh, Phase change material-based nano-cavity as an ef fi cient optical modulator, Nanotechnology 32 (2021), 095207.

[47] S.K. Chamoli, G. Verma, S.C. Singh, C. Guo, Phase change material based hot electron photodetection, Nanoscale 13 (2021) 1311–1317, https://doi.org/10.1039/d0nr06456d.

[48] Y.A. Cengel, Heat Transference a Practical Approach, vol. 4, MacGraw-Hill, 2004, p. 874, https://doi.org/10.1007/978-3-642-20279-7_5.

[49] H.C. Barshilia, N. Selvakumar, K.S. Rajam, A. Biswas, Spectrally selective NbAlN/NbAlON/Si3N4 tandem absorber for high-temperature solar applications, Sol. Energy Mater. Sol. Cells 92 (2008) 495–504, https://doi.org/10.1016/j.solmat.2007.11.004.

[50] W. Zhou, Y. Shen, E. Hu, Y. Zhao, M. Sheng, S. Wang, Y. Lee, C. Wang, D.W. Lynch, L. Chen, Nano-Cr-film-based solar selective absorber with high photo-thermal conversion efficiency and good thermal stability, Opt Express 20 (2012) 28953–28962.

[51] T.K. Tsai, Y.H. Li, J.S. Fang, Spectral properties and thermal stability of CrN/CrON/Al2O3 spectrally selective coating, Thin Solid Films 615 (2016) 91–96, https://doi.org/10.1016/j.tsf.2016.06.055.

[52] A.B. Khelifa, S. Khamlich, Z.Y. Nuru, L. Kotsedi, A. Mebrahtu, M. Balgouthi, A. A. Guizani, W. Dimassi, M. Maaza, Growth and characterization of spectrally selective Cr2O3/Cr/Cr2O3 multilayered solar absorber by e-beam evaporation, J. Alloys Compd. 734 (2018) 204–209, https://doi.org/10.1016/j.jallcom.2017.11.036.

[53] P. Li, B. Liu, Y. Ni, K.K. Liew, J. Sze, S. Chen, Large-scale nanophotonic solar selective absorbers for high-effi ciency solar thermal energy conversion, Adv. Mater. (2015) 4585–4591, https://doi.org/10.1002/adma.201501686.

[54] J. Wang, Z. Chen, D. Li, Simulation of two-dimensional Mo photonic crystal surface for high-temperature solar-selective absorber, Phys. Status Solidi A 1992 (2010) 1988–1992, https://doi.org/10.1002/pssa.200925573.

[55] J.B. Chou, Y.X. Yeng, A. Lenert, V. Rinnerbauer, M. Soljačić, E.N. Wang, S. Kim, Design of wide-angle selective absorbers/emitters with dielectric filled metallic photonic crystals for energy applications, Opt Express 22 (2014) 144–154, https://doi.org/10.1364/OE.22.00A144.

[56] F. Cao, D. Kraemer, T. Sun, Y. Lan, G. Chen, Z. Ren, Enhanced thermal stability of W-Ni-Al 2 O 3 cermet-based spectrally selective solar absorbers with tungsten infrared refl ectors, Adv. Energy Mater. (2014) 1–7, https://doi.org/10.1002/aenm.201401042.

[57] K. M, A.B. Harish, C. Barshilia, N. Selvakumar, K.S. Rajam, D.V. Sridhara Rao, Tandem absorber for high temperature solar selective applications, Appl. Phys. Lett. 191909 (2008) 1–4, https://doi.org/10.1063/1.2387897.

[58] K. Te Lin, H. Lin, T. Yang, B. Jia, Structured graphene metamaterial selective absorbers for high efficiency and omnidirectional solar thermal energy conversion, Nat. Commun. 11 (2020) 1–10, https://doi.org/10.1038/s41467-020-15116-z.

[59] C. Wu, B.N. Iii, J. John, A. Milder, B. Zollars, S. Savoy, G. Shvets, Metamaterial-based integrated plasmonic absorber/emitter for solar thermo-photovoltaic systems, J. Opt. 14 (2012), https://doi.org/10.1088/2040-8978/14/2/024005.

[60] Y. Zhu, H. Luo, C. Yang, et al., Color-preserving passive radiative cooling for an actively temperature-regulated enclosure, Light Sci. Appl. 11 (2022) 122, https://doi.org/10.1038/s41377-022-00810-y.